STRUCTURE-PROPERTY RELATIONSHIPS OF LITHIUM-ION BATTERY CATHODES USING STOCHASTIC 3D MODELING AND RESISTOR NETWORK SIMULATIONS BASED ON SYNCHROTRON TOMOGRAPHY

PHILLIP GRÄFENSTEINER[1,*], ALEXANDRA PAMPERIN[2], MARKUS OSENBERG[3],
RASMUS HIMSTEDT[4], MATTHIAS NEUMANN[5,6], BENEDIKT PRIFLING[1],
INGO MANKE[3], MARC KAMLAH[2], VOLKER SCHMIDT[1]

[1]*Institute of Stochastics, Ulm University, 89069 Ulm, Germany*

[2]*Institute for Applied Materials, Karlsruhe Institute of Technology,
76344 Eggenstein-Leopoldshafen, Germany*

[3]*Institute of Applied Materials, Helmholtz-Zentrum Berlin für Materialien und Energie,
Hahn-Meitner-Platz 1, 14109 Berlin, Germany*

[4]*Customcells Itzehoe GmbH, Fraunhoferstraße 1d, 25524 Itzehoe, Germany*

[5]*Institute of Statistics, Graz University of Technology, Kopernikusgasse 24/III,
8010 Graz, Austria*

[6]*Graz Center of Machine Learning, Rechbauerstraße 12, 8010 Graz, Austria*

Abstract. Macroscopic effective transport properties of battery materials are predominantly influenced by the morphology of their microstructure. In order to bridge the gap between these different length-scales, a stochastic 3D microstructure model is combined with physical simulations on the electrode scale. More precisely, the stochastic model is used to generate virtual, but realistic microstructures of cathodes in lithium-ion batteries. The model is calibrated to tomographic image data and validated with respect to various geometric descriptors and effective transport properties. By systematically varying the parameters of the model, a data base of artificial microstructures is created with varying volume fractions and size distributions of active material particles. Furthermore, a resistor network method is used to quickly compute the effective conductivity and effective diffusivity of these microstructures on the electrode scale, where the microstructure is represented by a simplified graph structure. Subsequently, the available data base is used to investigate quantitative structure-property relationships, which link geometric descriptors of the microstructure to effective transport properties of the electrode. Finally, the results are used to validate a previously established empirical formula that uses geometric descriptors of the microstructure to predict the effective conductivity.

Keywords. Stochastic 3D modeling, structure-property relationship, effective transport property, resistor network method, lithium-ion battery, synchrotron

1. Introduction

Lithium-ion batteries are one of the most dominating technologies for storing electrical energy due to their high energy density and capacity retention, leading to a plethora of applications ranging from electric vehicles to mobile devices [1]. However, due to the steadily increasing requirements, further technological progress is required to improve the electrochemical performance. In particular, it is well known that the 3D microstructure of electrodes in lithium-ion transition metal oxide batteries has a strong impact on the resulting electrochemical properties. Moreover, the 3D microstructure is strongly dependent on the underlying manufacturing

---

[*] *Corresponding author.* E-mail address: phillip.graefensteiner@uni-ulm.de

process. Thus, a deeper understanding of process-structure-property relationships is crucial in order to further optimize the electrochemical behavior. However, the manufacturing and imaging of a large number of electrode samples is expensive in time and costs, which means that extensive testing of varying production parameters and assessing the quality of the resulting electrodes is often an infeasible approach. These limitations can be overcome by an approach called virtual materials testing, in which digital twins of physical material samples are generated by means of a parametric stochastic 3D microstructure model, using methods of stochastic geometry [2, 3]. More precisely, tomographic image data of a small number of experimentally measured samples is used to estimate the parameters of the stochastic geometry model, which can then be used to generate virtual samples, where the morphology of their microstructure is statistically similar to that of the original sample. This process is validated by comparing various geometric descriptors between image data of experimentally measured electrodes and realizations of the calibrated model, see [4–8] for previous examples of stochastic microstructure modeling.

One of the main advantages of using a low-parametric stochastic geometry model is the ability to generate a wide range of virtual but realistic 3D microstructures by adjusting individual parameters of the model, just at the cost of computer simulations. In particular, it is possible to easily adjust the size distribution of active material particles and the final packing density, and thus to simulate virtual cathodes with markedly differing morphologies that can be physically recreated by adjusting corresponding production parameters during the manufacturing process. These virtually generated structures may then serve as geometry input for numerical simulations of macroscopic properties to investigate structure-property relationships [9–12].

One key transport property for assessing the performance of battery electrodes is the effective electronic conductivity, in case of the active material phase, or the effective ionic diffusivity, in case of the electrolyte phase, which are used to quantify the impact of the microstructure on the transport processes. Those are closely related to the M-factor [13] and the MacMullin number [14]. Classical approaches for computing this quantity involve numerically solving the Laplace equation on the discretized geometry, for which a variety of open-source software packages such as TauFactor [15], PuMA [16] or pytrax [17], and commercial software packages, such as GeoDict [18], Avizo [19] or Simpleware [20], are available. Another approach to quickly compute effective conductivity and diffusivity is the resistor network method (RNM) [21, 22], in which the microstructure is represented by a simplified graph structure. The RNM utilizes the well-known node potential method of electrical engineering and defines the active material particles or individual pore regions as potential nodes and the restriction to the respective flux, such as particle contacts or bottlenecks, as the resistances. Given this graph structure and specific resistances, one can efficiently compute the flux through the system and thus the effective transport property.

In a previous study [22], this approach was used to investigate structure-property relationships based on virtually generated assemblies of overlapping spheres. In the present paper, we aim to extend this approach to tomographic image data of experimentally measured and virtually generated cathodes in lithium-ion batteries. In particular, we estimate all necessary input information for RNM from binarized image data and do not rely on analytical knowledge of particle position and shape. The resulting values are compared to those obtained from classical approaches that solve the Laplace equation on the discretized geometry. Moreover, we also assess the quality of a previously established empirical regression formula [11], that uses geometric descriptors of the microstructure to predict the effective conductivity or diffusivity. Finally, we apply these approaches to the data base of virtually generated cathodes within the context of a variation study to further investigate the robustness of their predictive power.

The present paper is structured as follows. In Section 2, we describe the material as well as the acquisition and postprocessing of 3D image data considered in this study. In Section 3, the applied methods and the necessary concepts are stated. These consist of the stochastic

3D model for the generation of virtual microstructures in Section 3.1, the geometric descriptors used to characterize the morphology of the microstructures in Section 3.2, an introduction to the M-factor in Section 3.3, and the resistor network method and its application to discrete image data in Section 3.4. The results are presented in Section 4. In particular, we evaluate the fit of the virtually generated structures to tomographic image data in Section 4.1 by comparing the values of the above-mentioned geometric descriptors. In Section 4.2, we compare the estimates for the M-factor obtained by solving the Laplace equation and using the RNM, first for an idealized geometry of packed spheres, where analytical particle positions and radii are available, and second for experimentally measured tomographic image data of lithium-ion battery cathodes, as well as for realizations drawn from the stochastic 3D model fitted to measured image data. In Section 4.3, we use the parametric nature of the stochastic 3D model to vary the particle size distribution and the packing density, thereby generating various virtual microstructures that differ markedly in their morphology. Based on this database, structure-property relationships that link geometric descriptors of the microstructure to macroscopic effective transport properties are studied. In particular, we validate the previously established regression formula from [11] using the results from the RNM. Section 5 concludes.

2. Material and Imaging

2.1. **Material.** Three different cathode slurries were coated onto both sides of an aluminum substrate foil (15 µm thickness) using a doctor blade process. The difference between the three corresponding recipes is a slight change in the amount of conductive carbon additives. Apart from that, the cathode coatings consist of ∼97 w% lithium nickel manganese cobalt oxide (NMC83), ∼2 w% carbon black, and ∼1 w% polyvinylidene fluoride binder. More detailed information on the composition of additives is given in Table A1 of the Appendix. After the coating step, the produced electrodes were compressed to three different target densities during a calendering step, resulting in a total of 9 individual cathode coils. The achieved densities were calculated using the measured mass loadings and total thicknesses of the electrodes after calendering. Mass loadings were determined by weighing cut samples ($40\,\mathrm{mm}^2$) and subtracting the weight of the substrate foil. The thickness of the electrodes was measured with a dial gauge by Mitutoyo. The resulting values are shown in Table A2.

2.2. **Imaging.** We give an overview of the sample preparation, image acquisition and image processing techniques deployed in order to arrive at the data base of experimentally measured cathodes that is used for the results obtained in this study.

2.2.1. *Sample preparation.* Nine double-coated NMC cathode samples were prepared at the Helmholtz-Zentrum Berlin (HZB) following an identical protocol. Each electrode was cut into snippets of size $\sim 1\times 3\ \mathrm{mm}^2$ and fixed between plexiglas rods to ensure mechanical stability while avoiding adhesive ingress into the porous structure. The mounted specimens were transferred to the BAMline endstation [23, 24] at the BESSY II synchrotron of HZB for X-ray imaging.

2.2.2. *Synchrotron tomography (BAMline, BESSY II).* All measurements were performed at 30 keV using the BAMline's double multilayer monochromator. Projections were acquired in continuous-rotation (flyscan) mode over 180° with 2,500 projections per scan and 300 ms exposure time per projection. The imaging chain consisted of a CdWO_4 scintillator coupled to an Optique Peter microscope and a PCO.edge 5.5 sCMOS camera (2560×2160 pixels), resulting in an effective pixel size of 0.36 µm (field of view $\approx 922\,\mu\mathrm{m}\times 778\,\mu\mathrm{m}$).

2.2.3. *Data pre-processing and reconstruction.* Raw projection stacks were pre-processed prior to tomographic reconstruction. Flat-field corrections were applied before a total variation (TV) filter [25] was applied to the projection data for noise reduction. The parameters of the TV filter were tuned to suppress high-frequency noise while preserving edges that are critical for subsequent segmentation. Volume reconstruction was then performed with HZB in-house Python scripts based on the TomoPy framework [26] employing the gridrec filtered-backprojection algorithm [27]. Images were slightly rotated in Fiji [28] such that the current collectors of the measured cathodes are perpendicular to one of the main coordinate axes, as this is more convenient for selecting maximal cuboidal sampling windows and computing transport related descriptors along the direction of transport. See Figure 1a for an exemplary 2D slice of the grayscale image data.

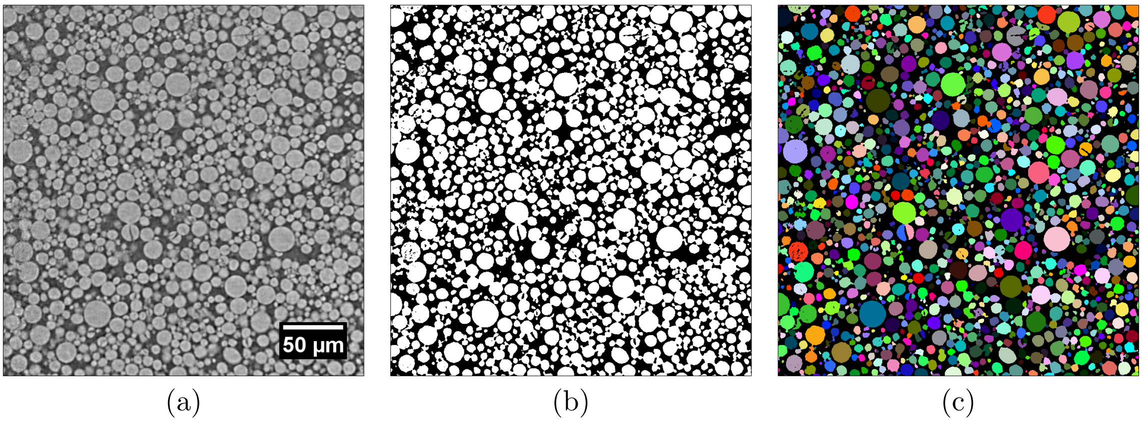

(a) (b) (c)

FIGURE 1. Exemplary 2D slice of tomographic image data: Grayscale (a) and binarized (b) image data, as well as a particle-discrete segmentation (c).

2.3. **Binarization.** The grayscale images described in Section 2.2 are further processed to obtain binary images, where the foreground phase corresponds to the active material particles. This is achieved by using a global thresholding on the 3D grayscale images, so that a desired volume fraction of the active material is reached. The desired volume fraction is determined based on knowledge of the slurry recipe and the measured calendering density of each of the cathodes, along with an estimate for the bulk density of the NMC83 active material particles. More precisely, the volume fraction of active material V_{AM} is given by

$$V_{\mathrm{AM}} = M_{\mathrm{AM}} \frac{d}{d_{\mathrm{AM}}}, \tag{1}$$

where M_{AM} is the mass weighted fraction of active material, known from the slurry recipe, d is the measured density of the cathode, see Table A2 of the Appendix, and d_{AM} is the bulk density of the active material, estimated to be equal to $4.95\,\mathrm{g\,cm^{-3}}$. Note that the mass weighted fraction of active material is equal to the mass weighted fraction of active material within the slurry, as the pore space has no mass. The mass weighted recipes along with the measured densities of each cathode are given in the Appendix. Based on Eq. (1), the volume fraction of active material is determined for each cathode. Using the histogram of grayscale values, we can determine the appropriate threshold such that the resulting binary images have the desired volume fraction of active material, see Figure 1b.

2.4. **Particle-discrete segmentation.** The binary image data is processed again in order to achieve a particle-discrete segmentation, which assigns a label to all voxels in D based on which particle they belong to. Voxels with the same label belong to the same particle, whereas voxels that do not belong to any particle receive the label 0, indicating a background voxel.

Let $B\colon D \to \{0,1\}$ be a binary image defined over some domain $D \subset \mathbb{Z}^3$, with $\mathbb{Z} = \{\ldots,-1,0,1,\ldots\}$, where voxels with the value 0 and 1 correspond to background and active material voxels, respectively. At first, we apply a morphological closing [29] to the foreground phase of the image B to close small holes or cracks in the active material particles, as these can negatively affect the further segmentation procedure and lead to over segmentation. The structuring element for this morphological closing was chosen to be a sphere with a radius of 2 voxels (0.72 µm). We now employ a marker-based watershed algorithm [30] to receive a particle-discrete segmentation of the closed image. In particular, we use an adaptation of this algorithm as proposed in [31] in order to reduce over-segmentation. Here, morphological reconstruction [32, 33] is applied to the Euclidean distance transform [34] of the binary image to reduce the amount of local maxima. The severity of this reduction is controlled by a parameter $\alpha > 0$, for which a value of $\alpha = 0.12$ was chosen. The remaining local maxima of the reconstructed distance transform are used as markers for the watershed algorithm.

The resulting particle-discrete segmentation assigns each voxel to a particle and contains no more information about the background. Therefore, it is multiplied voxel-wise with the original binary image B in order to re-classify background voxels and ensure that they retain a value of 0. Subsequently, labels containing less than 100 voxels ($\approx 4.67\,\mu\mathrm{m}^3$) are discarded (the labels of these voxels are set to 0), as they do not resemble regions that are meaningful to our analysis and are likely due to remaining over-segmentation.

We are now left with an image $S\colon D \to \{0, 1, 2, \ldots\}$ that assigns the value 0 to background voxels and a positive integer to active material voxels that is unique to the particle to which they belong. However, this segmentation still contains so-called watershed lines. That is, wherever two regions are connected in the original binary image B, the voxels along the boundary of the two regions are assigned as background voxels. Thus, we assign each boundary voxel to one of its neighboring particles as follows. The final label of a voxel $v \in D$ at a watershed line, where two neighboring particles meet, is determined based on the neighboring voxels of v, where we always consider voxel connectivity with respect to the 26-neighborhood. More precisely, all non-background voxels which are connected to v and their corresponding shortest distances to the background are computed. The final label of v is given by the label of the particle that has the largest shortest distance to the set of background voxels. An exemplary 2D slice of the final particle-discrete segmentation is shown in Figure 1c.

3. METHODS

3.1. **Stochastic 3D microstructure model.**

The general framework for the stochastic 3D model of systems of active material particles deployed in this study has been proposed in [35], while the specific implementation used in the present paper follows [36]. The complement of the thereby generated active material phase will then represent the union set of binder-additives and pores, which we loosely refer to as the pore phase. Since the model has already been described in detail in [35, 36], we only give a brief summary of some necessary information.

Periodic boundary conditions are respected during all parts of the model construction described in Sections 3.1.1 to 3.1.3 below. The values of estimated model parameters are given in Section A.2 of the Appendix. Furthermore, in the context of a virtual scenario analysis, the size distribution and the packing density of the active material particles will be systematically varied, see Section 4.3. Figure 2 shows 3D-renderings of both tomographically measured image data and simulated image data drawn from the fitted stochastic microstructure model.

3.1.1. *Placeholder sphere system.*

In a first step, a spatial arrangement of placeholder spheres is constructed that indicates the position and size of active material particles, which are later replaced by realistic particle shapes. Let $W \subset \mathbb{R}^3$ denote a cuboidal sampling window and let $P\colon (0, \infty) \to (0, \infty)$ denote the probability density function of the sphere radii. Additionally, let $p \in (0, 1)$ denote the targeted packing density, *i.e.*, the targeted volume fraction of active material within the sampling window W. The placeholder sphere system is generated by drawing radii repeatedly from the probability density P until the total volume of all spheres exceeds the value of the product $p\nu_3(W)$, where $\nu_3(W)$ denotes the volume of W. The spheres generated in this way are spatially arranged within W placing their centers according to the uniform distribution on W. This initial (overlapping) configuration of spheres is then rearranged by

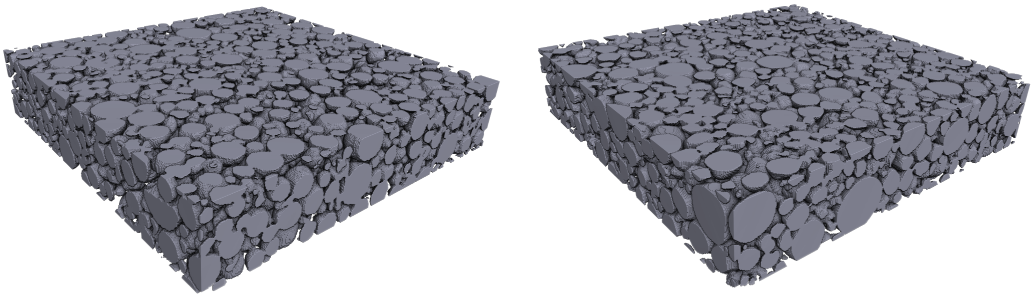

FIGURE 2. Left: Binarized tomographic image data. Right: Model realization. The physical size of the cutouts is $144{\times}144{\times}36\,\mu\mathrm{m}^3$. The active material is visualized in gray, while the binder-additive phase and pores are transparent.

a force-biased algorithm [37, 38] to achieve a non-overlapping sphere system. Subsequently, a neighborhood graph is determined to control the contact between spheres, where the set of vertices is given by the centers of spheres and edges are added between pairs of spheres that are within a given distance threshold $d > 0$ from each other. This neighborhood graph is then used to condition the generation of realistic particle shapes on the fact that there should be a connection between particles that share an edge. Adjusting the value of d therefore affects the connectivity of the final particle system.

3.1.2. *Modeling the outer particle shape.* The non-spherical outer shape of the active material particles is modeled by an isotropic Gaussian random field $X = \{X(\theta,\phi), (\theta,\phi) \in [0,\pi]\times[0,2\pi)\}$ on the unit sphere, where this modeling approach assumes that individual particles are star-shaped, *i.e.*, there exists a so-called star-point within each particle from which all straight lines to the boundary are completely contained within the particle. After fixing such a star-point for each particle, the value of $X(\theta,\phi)$ can be interpreted as the random distance from the star-point to the boundary of the particle along the direction given by the polar coordinates $(\theta,\phi) \in [0,\pi] \times [0,2\pi)$. The random field X is uniquely defined by its mean value $\mu > 0$ and its angular power spectrum $A = \{A_\ell, \ell \in \mathbb{N}_0\}$, where $A_\ell > 0$ for each $\ell \in \mathbb{N}_0 = \{0,1,\ldots\}$. Namely, it holds that

$$X(\theta,\phi) = \sum_{\ell=0}^{\infty} \sum_{m=-\ell}^{\ell} a_{\ell,m} Y_{\ell,m}, \tag{2}$$

for each $(\theta,\phi) \in [0,\pi] \times [0,2\pi)$, where $Y_{\ell,m}\colon [0,\pi] \times [0,2\pi) \to \mathbb{C}$, with $\mathbb{C}$ denoting the complex plane, $\ell \in \mathbb{N}_0$ and $m \in \{-\ell,\ldots,\ell\}$, are the so-called spherical harmonics, and $\{a_{\ell,m},\ \ell \in \mathbb{N}_0,\ m \in \{-\ell,\ldots,\ell\}\}$, is a sequence of complex-valued, independent Gaussian random variables. More precisely, it holds that $\operatorname{Re} a_{\ell,m}$ and $\operatorname{Im} a_{\ell,m}$ are independent and $\mathcal{N}(0, A_\ell/2)$ distributed for $\ell \in \mathbb{N}_0$ and $m \in \{-\ell,\ldots,-1,1,\ldots,\ell\}$, where $\mathcal{N}(\mu,\sigma^2)$ denotes the normal distribution with mean value μ and variance σ^2. Furthermore, $a_{\ell,0}$ is real-valued with distribution $\mathcal{N}(0, A_\ell)$ for $\ell \in \mathbb{N} = \mathbb{N}_0 \setminus \{0\}$, whereas $a_{0,0}$ has the distribution $\mathcal{N}(2\mu\sqrt{\pi}, A_0)$, see [39] for more details. The random field X can therefore be approximated by truncating the series expansion in Eq. (2) at some $L \in \mathbb{N}$, requiring only few values of the angular power spectrum A to be estimated from tomographic image data, and μ which is the mean value of the probability density P of sphere radii.

3.1.3. *Conditional simulation of Gaussian random fields.* For each particle, we can draw a realization of the Gaussian random field X and use it to insert the realistic particle shape at the location of the corresponding placeholder sphere within the sampling window W, where the realizations of $X(\theta,\phi)$ must be conditioned on $X(\theta,\phi) > 0$ for all $(\theta,\phi) \in [0,\pi] \times [0,2\pi)$ to generate realistic particle shapes. In practice, this is only an issue for particles with a small mean radius $\mu > 0$ and can be achieved by rejecting and re-sampling realizations with $X(\theta, \phi) \leq 0$ for some $(\theta, \phi) \in [0, \pi] \times [0, 2\pi)$. The random fields of particles that are adjacent in the neighborhood graph described in Section 3.1.1 are additionally conditioned on overlapping at a particular point between the two spherical placeholder particles, see Eq. (1) in [36], which ensures that these particles are then connected in the resulting 3D microstructure. This additional conditioning of Gaussian random fields does not significantly increase the complexity of the simulation algorithm, since the multivariate normal distribution of a Gaussian random vector that is conditioned on some of its components assuming specific values still follows a multivariate normal distribution whose mean vector and covariance matrix can be explicitly determined [40].

3.1.4. *Discretization and post-processing.* In theory, realizations of the stochastic 3D microstructure model described above are subsets within a continuous domain $W \subset \mathbb{R}^3$, which are then discretized on the lattice $D = W \cap \mathbb{Z}^3$ to generate voxelized 3D image data, where $\mathbb{Z} = \{\ldots, -1, 0, 1, \ldots\}$. Furthermore, in order to promote more realistic (not too narrow) bottlenecks between two touching particles, a post-processing step is applied that consists of Gaussian blurring with standard deviations $\sigma_x = \sigma_y = \sigma_z = 0.36\,\mu\text{m}$ followed by Otsu thresholding [41]. Finally, a correction factor $\rho \in (1, 1.01)$ is used to scale the radii of the placeholder spheres, to meet a desired volume fraction, as this can vary from the originally targeted volume fraction due to the above-mentioned post-processing step. For more information on the model itself and the estimation of model parameters from tomographic image data, see [36].

3.2. **Geometric descriptors.** The stochastic 3D model introduced in Section 3.1 represents the union of all active material particles as a stationary random set in $\mathbb{R}^3$, denoted by $\Xi \subset \mathbb{R}^3$ in the following. To analyze the morphology of such random sets and, in particular, to formulate structure-property relationships in a quantitative manner, various geometric descriptors of stationary random sets are considered in the literature. Furthermore, these descriptors are used to validate the goodness of model fit with respect to experimentally measured image data. We briefly explain four different geometric descriptors of stationary random sets considered in this study and show how they can be estimated from binarized image data given in some domain $D \subset \mathbb{Z}^3$.

3.2.1. *Volume fraction.* The volume fraction of a stationary random set $\Xi \subset \mathbb{R}^3$ is the expected volume $\varepsilon = \mathbb{E}\nu_3(\Xi \cap [0,1]^3)$ of Ξ per unit volume. Thus, $\varepsilon \in [0, 1]$. This quantity can be estimated from binarized image data in D simply by counting the number of foreground voxels in D and dividing it by the total number of voxels in D, see Section 6.4.2 in [2].

3.2.2. *Specific surface area.* This quantity will be denoted by S_V in the following. It is defined as the expected surface area $S_V = \mathbb{E}(\mathcal{H}(\partial\Xi \cap [0,1]^3)$ of Ξ per unit volume, where $\mathcal{H}$ denotes the two-dimensional (Hausdorff) surface measure in $\mathbb{R}^3$ and $\partial\Xi$ is the boundary of Ξ. In order to estimate S_V from binary image data, we use an algorithm proposed in [42], which is based on weighted 2×2×2 neighborhoods.

3.2.3. *Constrictivity.* In order to quantify the strength of bottleneck effects within the stationary random set Ξ, we consider the two characteristic radii $r_{\max}$ and $r_{\min}$. For the former, we consider the continuous phase size distribution function $\mathrm{CPSD}\colon [0, \infty) \to [0, 1]$, where $\mathrm{CPSD}(r)$ is the volume fraction of Ξ after a morphological opening [29] with radius $r > 0$. The morphological opening of Ξ with radius r is the subset of Ξ that can be covered by spheres of radius r being completely contained within Ξ. We then put $r_{\max} = \sup\{r \geq 0\colon \mathrm{CPSD}(r) \geq 0.5\}$, *i.e.*, $r_{\max}$ is the largest radius that can be used to cover at least half the volume of Ξ by spheres of that radius. The value of $r_{\min}$ is defined similarly, except that the covering spheres must intrude the set Ξ from a predefined direction. Thus, we require half of the volume of Ξ to be coverable and reachable by spheres of radius $r_{\min}$ that are completely contained within Ξ. In the present paper, to define the radius $r_{\min}$, we always consider spheres intruding along the thickness direction of the cathode material described in Section 2.1. This choice is motivated by the physical experiment of mercury intrusion porosimetry, and the radius $r_{\min}$ can be considered as the radius of the typical bottleneck [11]. Finally, we use the radii $r_{\max}$ and $r_{\min}$ to define the constrictivity $\beta = r_{\min}^2/r_{\max}^2$. Thus, $\beta \in [0,1]$, where values of β closer to 1 indicate fewer bottleneck effects. To estimate β from binary image data, the values of $r_{\max}$ and $r_{\min}$ can be estimated using morphological opening and the Euclidian distance transform [29, 34].

3.2.4. *Mean geodesic tortuosity.* Although many different notions of tortuosity are known and used throughout the literature [13], we focus on the mean geodesic tortuosity in this paper. For a given transport direction and a given material phase represented by a stationary random set $\Xi \subset \mathbb{R}^3$, we consider two (parallel) source and sink planes, e.g., on opposite sides of some cuboidal domain $W \subset \mathbb{R}^3$. Then, the mean geodesic tortuosity τ is defined as the expected length of the shortest paths from starting points in the source plane that belong to the given phase, through that phase to the sink plane (under the condition that such paths exist), normalized by the distance between the source and sink planes along the transport direction. The mean geodesic tortuosity τ defined in this way can be estimated from binarized image data by using Dijkstra's algorithm [43] to compute the shortest paths and subsequently averaging the lengths of all these shortest paths for all voxels that belong to the given phase within the source plane. In this paper, we always consider transport along the thickness direction of the cathode material.

3.3. **Macroscopic transport properties.** To quantify the impact of 3D microstructure on macroscopic transport properties, such as ion diffusion or electron conduction, we consider the so-called M-factor [13], which is defined by the ratio

$$M = \frac{k_{\text{eff}}}{k_{\text{bulk}}} \tag{3}$$

of effective conductivity k_{eff} to bulk conductivity k_{bulk} of the active material phase or, analogously, effective over bulk diffusivity in the case of the pore phase. For simplicity, we will use the term conductivity even when referring to transport through the pore phase. The M-factor takes its values within the unit interval $[0,1]$ and describes a normalized effective conductivity of the given material phase, isolating the influence of the microstructure on transport processes from the bulk conductivity of the material. In the present paper, the effective conductivity k_{eff} is determined using the resistor network method, see Section 3.4 below, and k_{bulk} is assumed to be equal to 1. Equivalently, the M-factor can be determined by the formula

$$M = \frac{V_{\text{frac}}}{\tau_{\text{eff}}}, \tag{4}$$

where V_{frac} is the volume fraction of the considered phase, and τ_{eff} is its effective tortuosity. The value of τ_{eff} is determined by solving the partial differential equation corresponding to the steady-state diffusive flow through the domain defined by the considered phase using the Matlab application TauFactor [15]. In the following, we will consider the values of the M-factor computed by means of Eq. (4) as ground truth.

3.4. **Resistor network method.** We now give a brief introduction to the resistor network method (RNM) for quickly computing the effective conductivity k_{eff}, where the underlying model operates on a graph structure that can be determined from binarized image data. In Section 3.4.1, we explain this procedure in detail. Since the RNM itself has already been used in various previous papers, see e.g. [21, 22], in Section 3.4.2 we just give a brief overview of this method.

3.4.1. *Connectivity graph of active material particles.* In this section, we describe how to construct a connectivity graph, on which the RNM operates, from a particle system observed in binarized image data. This graph encodes information about the location of each particle within its nodes, whereas information about the connection between two neighboring particles is contained within its edges.

The starting point of this procedure is a particle-discrete segmentation. That is, we assume that we are given a labeled image $S\colon D \to \{0,1,2,\ldots\}$, defined in some domain $D \subset \mathbb{Z}^3$, where voxels $v \in D$ such that $S(v) = 0$ represent the background, and voxels $u, v \in D$ with $S(u) = S(v) \neq 0$ belong to the same particle. Then, we consider a connectivity graph $\mathcal{G} = (\mathcal{V}, \mathcal{E})$, where $\mathcal{V} \subset \mathbb{R}^3$ is a set of vertices, and $\mathcal{E} \subset \big\{(\{u,v\}, s)\colon u, v \in \mathcal{V}, s \geq 0\big\}$ is a set of weighted undirected edges. Each vertex corresponds to an individual particle identified by the underlying particle-discrete segmentation, and each undirected edge between two vertices indicates that the corresponding particles are connected in the underlying image data. Recall that we always consider voxels connectivity in image data with respect to the 26-neighborhood. The weight $s \geq 0$ of an edge $(\{u,v\}, s) \in \mathcal{E}$ is the contact area between the two particles corresponding to the vertices u and v, which is crucial information used in the RNM.

More precisely, the graph $\mathcal{G}$ is constructed as follows. Let $j \in \mathbb{N}$ be an integer such that the set $S^{-1}(j) = \{v \in D : S(v) = j\}$ is not empty and connected to at least one other non-empty set $S^{-1}(k) \subset D$, for some $k \in \mathbb{N}$ with $k \neq j$. We then determine the barycenter $v_j \in \mathbb{R}^3$ of $S^{-1}(j)$ and add it to the vertex set $\mathcal{V}$. We repeat this procedure for each (positive) label in $S(D) \setminus \{0\} \subset \mathbb{N}$ so that each non-isolated particle receives a corresponding vertex in the connectivity graph. Subsequently, vertices $v_j, v_k \in \mathcal{V}$ with $v_j \neq v_k$ that correspond to connected voxel sets $S^{-1}(j), S^{-1}(k) \subset D$ receive a weighted edge $(\{v_j, v_k\}, s) \in \mathcal{E}$ in the graph $\mathcal{G}$. To estimate the contact area $s \geq 0$ from discretized image data, we use the algorithm provided in [42], which relies on weighted 2×2×2 neighborhoods. More precisely, we apply this algorithm three times to estimate the surface area of the sets $S^{-1}(j)$, $S^{-1}(k)$, and $S^{-1}(j) \cup S^{-1}(k)$. Then, using the inclusion-exclusion principle, see Chapter I in [44], for the two-dimensional (Hausdorff) surface measure in $\mathbb{R}^3$, we can infer the contact area s between the particles corresponding to the voxel sets $S^{-1}(j)$ and $S^{-1}(k)$.

In some cases, where the contact area between two particles is very small, the value of s estimated in this way can become negative, which is due to discretization artifacts. As this occurs only for very small contact areas, we simply set the contact area s to 0 in this case. Finally, we add an edge $(\{u,v\}, s)$ to $\mathcal{E}$, where s is the estimated contact area between the two connected particles corresponding to $u, v \in \mathcal{V}$.

In addition to the contact areas provided in the connectivity graph, we also determine the contact areas between particles and the boundary box of the image domain D. That is, for any particle touching one or multiple boundary surfaces, we sum up the area of all voxel faces that are in contact with that surface.

3.4.2. *Resistor networks.* The resistor network method uses connectivity graphs, like that constructed in Section 3.4.1, to quickly determine the effective conductivity k_{eff} appearing in Eq. (3) for both the active material phase and the electrolyte-filled pores. Note that both the three-dimensional stationary electrical flux in the active material and the stationary ionic flux in the electrolyte are divergence free, satisfying $\nabla \cdot F = 0$, with F being the respective flux. Additionally, the driving forces of the said fluxes can be reduced to a potential gradient and a concentration gradient using Ohm's law and Fick's law, respectively. Since mathematically there is no difference between these transport phenomena [45, 46], we can use a single method to solve for the respective transport in both phases.

For the active material phase, this involves assigning a resistance to every contact between two connected particles based on purely geometric bottleneck effects. That is, for connected particles corresponding to the vertices $u, v \in \mathcal{V}$ within the connectivity graph stated in Section 3.4.1, the resistance R_{uv} of the particle contact is given by

$$R_{uv} = \frac{\dfrac{1}{k_u} + \dfrac{1}{k_v}}{4r_c}, \tag{5}$$

where $r_c > 0$ is the contact radius between the two particles and k_u and k_v are the material (bulk) conductivities of the particles, which are assumed to be equal to 1 in this paper. In case of spherical particles, r_c is the radius of the contacting circle, while for non-spherical particles it is the radius of an area-equivalent circle. The resistances R_{uv} given in Eq. (5) enter a system of linear equations according to Kirchhoff's law in order to determine the effective conductivity k_{eff} of the active material phase, see [21, 22] for a more detailed description.

Note that the value of r_c can be determined using analytical information about the centers and radii of spherical particles, or estimated from tomographic image data as described in Section 3.4.1. As shown in [21], the former method is in good agreement with other methods for determining the effective conductivity but is not applicable to tomographic image data due to the required analytical information.

For the electrolyte-filled pore phase, a Laguerre tessellation [47] is used to determine individual pore regions. Similarly to the solid phase of active material, resistances are assigned to each pair of neighboring pore regions, which are then arranged into a system of linear equations to determine the effective conductivity k_{eff} of the pore phase. These resistances are determined on the basis of a multi-step procedure, which is detailed in [22]. Crucially, the determination of the effective conductivity of the pore phase does not require any information of contact areas and is therefore less sensitive to the estimation of surface areas from tomographic image data.

4. RESULTS

4.1. **Model fitting and statistical data analysis.** To fit the stochastic 3D microstructure model summarized in Section 3.1 to experimentally measured tomographic image data, we use the geometric descriptors stated in Section 3.2, see Section A.2 for more details. For this purpose, we order the nine cathode samples considered in this study with respect to their volume fraction of active material, computed from measured calendering densities as described in Section 2.3. These values were also used for the packing density $p \in (0, 1)$ of the stochastic 3D model to generate 10 discretized model realizations of size $500 \times 500 \times 100$ voxels for each of the model specifications corresponding to the nine cathode samples. Furthermore, for each of the nine samples, the tomographic image data has been subdivided into 25 slightly overlapping cutouts with a size of $557 \times 557 \times 122$ voxels. Then, for both kinds of (simulated and measured) image data, geometric descriptors are estimated as described Section 3.2.

Figure 3 shows box plots indicating the distribution of the estimated values for every sample. In particular, Figure 3a shows box plots of the values obtained for the volume fraction ε of the solid phase. We expect the box plots of this descriptor to match quite nicely for simulated and measure image data, as it is largely controlled by the packing density p used in the stochastic 3D model. However, the tomographic image data exhibit a wider spread in estimated values of ε than the realizations of the stochastic model. Note that for the tomographic image data, the mean values of the estimated volume fractions do not necessarily coincide with the global packing density due to the slight overlap of the 25 cutouts used to estimate this descriptor.

The estimated values of the specific surface area S_V are visualized in Figure 3b. These values show high agreement for the simulated and measured image data for most samples, except for the one with the highest volume fraction of the solid phase. For this sample, the estimated specific surface area of the tomographic image data discontinues its monotonous trend and suddenly decreases, yielding to a larger discrepancy between the values obtained for tomographic image data and model realizations, respectively. A similar effect has been observed in the case of polymer batteries that reach a maximum specific surface area for approximately 60% volume fraction of the solid phase [48].

The values obtained for mean geodesic tortuosity τ agree well for the pore phase, but show a slight decrease for model realizations compared to the image data for experimentally measured cathodes. This likely causes the correspondingly increased values of the M-factor and the effective conductivity k_{eff} determined by the RNM, see Figures 3c, 3d and 3f.

The values obtained for the constrictivity β of the solid phase match well, whereas the values of β for the pore phase are slightly lower for model realizations compared to experimentally measured cathodes. Similarly to the influence of the mean geodesic tortuosity τ, this likely causes the correspondingly decreased values of the M-factor and the effective conductivity k_{eff}, see Figures 3c, 3e and 3f. These connections are also in line with the relationship between ε, β and τ discussed later in Section 4.4. Importantly, the stochastic 3D model stated in Section 3.1 is able to generate microstructures that are similar to those of experimentally measured cathodes, with respect to both their morphology characterized by geometric descriptors and their functional response quantified through the M-factor and the effective conductivity k_{eff} determined by the RNM.

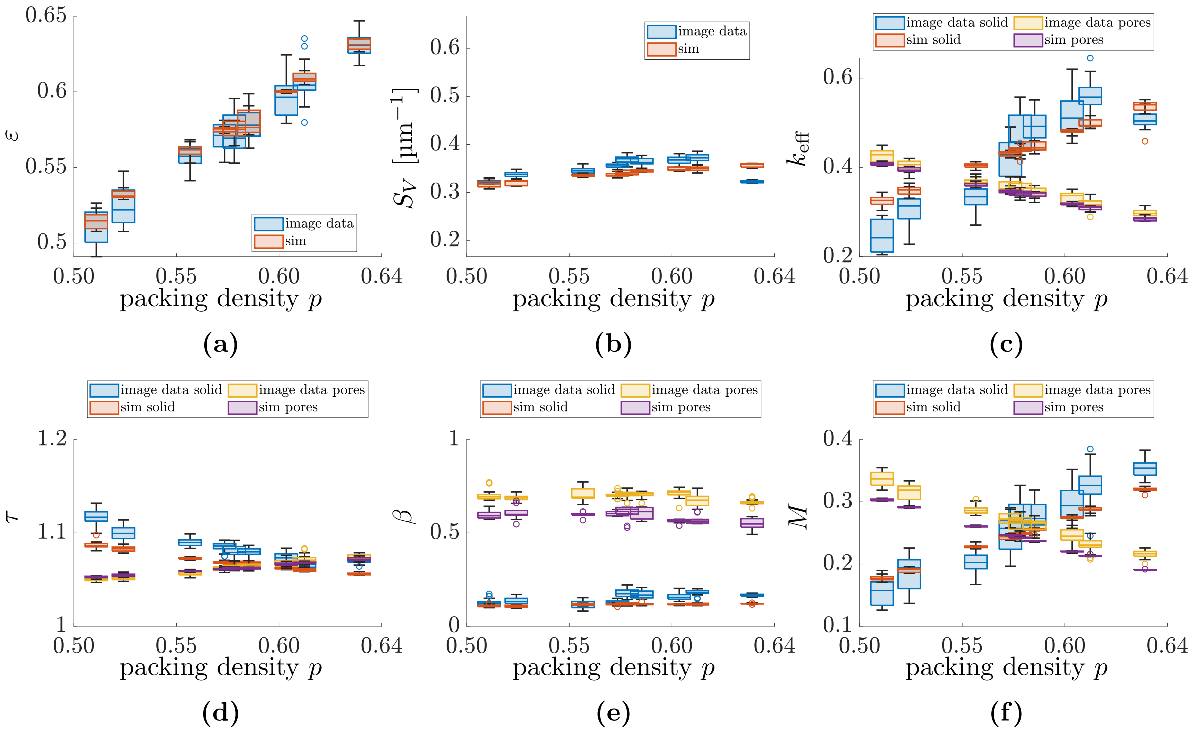

(a) (b) (c)

(d) (e) (f)

FIGURE 3. Geometric descriptors and effective properties determined for realizations of the stochastic 3D model and for cutouts of tomographic image data. Depicted are the volume fraction of the solid phase (a) and its specific surface area (b), the effective conductivity of solid and pore phase determined by the RNM (c), their mean geodesic tortuosity (d) and constrictivity (e), as well as their M-factor determined by the Matlab application TauFactor (f).

4.2. **TauFactor versus RNM.** In this section, we compare the values obtained for the M-factor as computed by the Matlab application TauFactor and the RNM, respectively. First, in Section 4.2.1, we investigate this question for idealized particle systems of perfect shperes, and subsequently, in Sections 4.2.2 and 4.2.3, for experimentally measured tomographic image data and for realizations drawn from the stochastic 3D model fitted to this data.

4.2.1. *Systems of overlapping spheres.* We first consider idealized particle systems where all particles are perfect spheres. To generate such structures, we use a sphere packing algorithm proposed in [49, 50] that generates a random overlap-free packing of spheres with a given radius distribution. We then follow the procedure described in [22] to force contact between spheres and densify the structure, where the spheres are moved stress-free in the thickness direction relative to their starting position until a target mean contact angle (mca) is reached. For a given pair of overlapping spheres, the contact angle is the maximum of the two angles enclosing the contact radius of the two spheres. Subsequently, the sphere systems are discretized into voxelized image data at a size of 500×500×500 voxels, see Figure 4a for an example of a planar 2D slice. In this way, a total of eight sphere systems, each consisting of 1000 overlapping spheres, was generated with varying radius distributions and mean contact angles. The radius distributions of the spheres were chosen so that the sizes of the discretized spheres (in voxels) are comparable to those observed in experimentally measured tomographic image data, see Table A4 in Appendix A.3 for a detailed list of the parameters used to generate the sphere systems.

The advantage of such an idealized particle system is that in this setting, the analytical positions and radii of the spherical particles are available, and thus their contact areas can be determined analytically. On the other hand, we can estimate the values of these areas using the corresponding discretized image data. We can therefore compare three different ways of determining the M-factor: (i) by the Matlab application TauFactor, (ii) by the RNM using analytically determined contact areas (analytical RNM), and (iii) by the RNM using contact areas estimated from discretized image data (discretized RNM). Figures 4b and 4c show an overview of the results obtained. For the solid phase, we can see in Figure 4b that although the values determined by analytical RNM and TauFactor agree relatively well, the values determined by discretized RNM deviate significantly from those obtained by the other two methods. Note that the differences between the values determined by the discretized and analytical RNM, respectively, can be mainly attributed to the uncertainty in estimating the sizes and contact areas of the spheres from discretized image data. A comparison of the distributions of contact areas resulting from discretized and analytical RNM is visualized in Figure A1 of Appendix A.3, which shows a consistent overestimation of analytically determined contact areas. For the pore phase, the values of the M-factor obtained by the discretized and analytical RNM are much closer to each other, whereas there is a slightly more noticeable deviation from the values obtained by TauFactor, see Figure 4c. Recall that the RNM approach to the computation of the effective conductivity in the pore phase does not rely on contact areas. Instead, a Laguerre tessellation is used to decompose the pore phase into individual pore regions, which is fundamentally different from the TauFactor approach and could explain the deviations between the results obtained by analytical RNM and TauFactor for the pore phase.

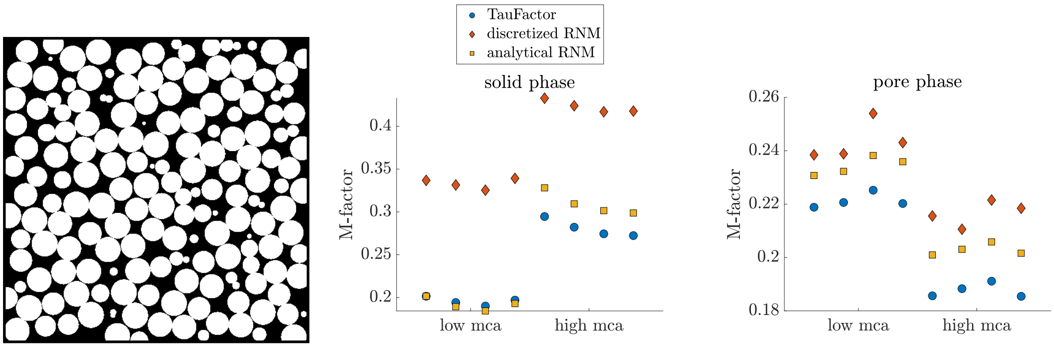

(a) (b) (c)

Figure 4. 2D slice of a densely packed system of overlapping spheres (a). Values of the M-factor determined by TauFactor (blue circles), analytical RNM (yellow squares) and discretized RNM (orange diamonds) for the solid phase (b) and the pore phase (c).

4.2.2. *Comparison on tomographic image data.* We are now extending the comparative analysis conducted above from idealized geometries to experimentally measured tomographic image data. In this case, no analytical contact areas are available, so we can only compare the values obtained for the discretized RNM to those of TauFactor.

Figure 5a shows the values of the M-factor obtained by both TauFactor and the RNM for the 9×25=225 overlapping cutouts taken from the nine 3D images of experimentally measured cathodes. We observe a small deviation for the values of the pore phase and a moderate deviation for the values of the solid phase. Similarly to the scenario discussed in Section 4.2.1, we attribute these deviations to the uncertainty of estimating particle sizes and contact areas from discretized image data.

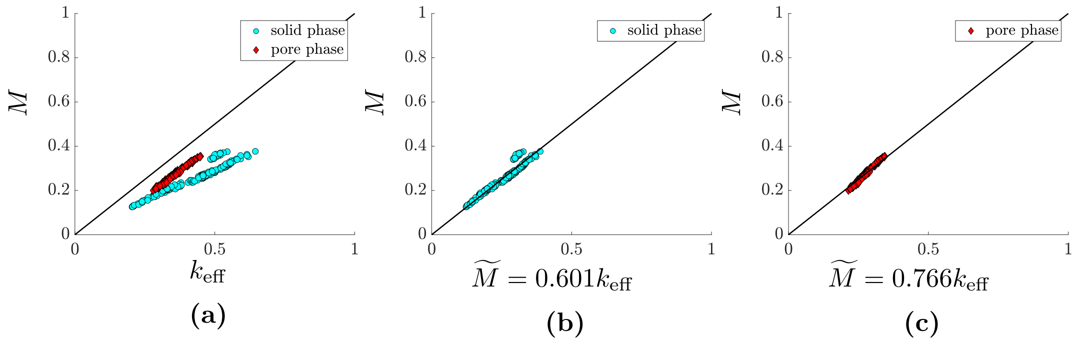

(a) **(b)** **(c)**

FIGURE 5. Values of the M-factor determined by TauFactor versus those obtained by RNM for cutouts of tomographic image data. Shown is a direct comparison (a) as well as two linear fits obtained for values of the solid phase (b) and the pore phase (c).

However, it turns out that these deviations can be easily corrected. Figures 5b and 5c show linear fits of the form

$$\widetilde{M} = c k_{\text{eff}} \tag{6}$$

of the values of k_{eff} obtained by RNM to the values obtained by TauFactor using Eq. (4), where $c > 0$ is some coefficient determined using the least-squares method. This approach has also been used in [10] to adjust the predictions of a graph-based pore network model to be more in line with more involved numerical simulations. The value of c is estimated separately for the solid and the pore phase, resulting in $c = 0.601$ and $c = 0.766$, respectively. These values are similar to those obtained for the case of idealized geometries in Section 4.2.1. For the data visualized in Figure 4, we obtained an average factor between discretized RNM and TauFactor of 0.6257 for the solid phase and 0.8876 for the pore phase. This suggests that the discrepancy between TauFactor and RNM results is not influenced by transferring the methods from image data of idealized geometries to experimentally measured tomographic image data of lithium-ion battery cathodes, but is instead caused by the natural difficulties of accurately estimating particle positions and contact areas from voxelized image data.

4.2.3. *Comparison on model realizations.* Finally, we also compare the M-factor values obtained by RNM and TauFactor for realizations of the stochastic 3D model fitted in Section 4.1 to measured image data. In particular, we discuss the fit of $\widetilde{M}$ as defined in Eq. (6) using the values of c obtained for the solid and pore phase based on tomographic image data as described in Section 4.2.2.

Figure 6 summarizes the results in the same way as Figure 5. Note that, in a different form, these results were already presented in Figures 3c and 3f as part of the model validation, which showed slight discrepancies between the M-factor values of model realizations and those of tomographic image data. Nevertheless, the scatter plots in Figures 6b and 6c show that the gap between the M-factor values determined by RNM and by TauFactor can be corrected by using in Eq. (6) the same constant c for both the solid and the pore phase, independently of whether the underlying data has been measured experimentally or generated virtually.

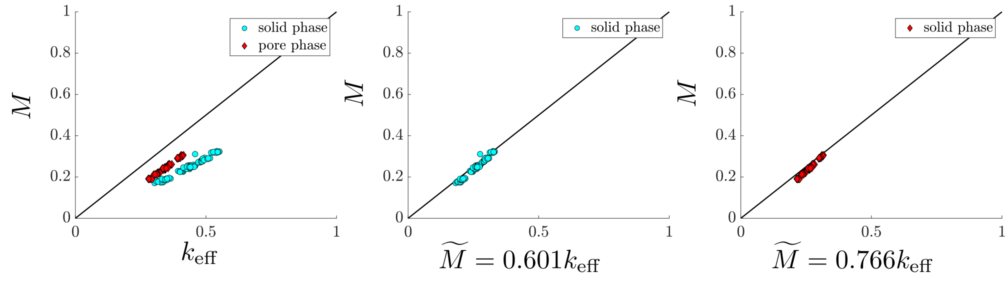

(a) **(b)** **(c)**

FIGURE 6. M-factor values determined by TauFactor versus those obtained by RNM for realizations of the stochastic 3D model. Shown is a direct comparison (a) as well as the two linear fits that use the same values for c as those obtained based on cutouts of tomographic image data for values of the solid phase (b) and the pore phase (c).

4.3. **Generating a data base of virtual cathodes.** As demonstrated in Section 4.1, using the stochastic 3D model considered in the present paper, we are able to generate virtual electrode structures that closely resemble those measured by tomographic imaging. Moreover, due to the parametric nature of the stochastic 3D model, we can purposefully vary individual aspects of these virtual structures in order to generate realistic alterations of the structures observed in tomographic image data. In particular, we will focus on varying two parameters of the placeholder sphere system considered in Section 3.1.1: the probability density function $P\colon (0,\infty) \to (0,\infty)$ of the sphere radii and the targeted packing density $p \in (0,1)$.

The packing density p is varied within the set $\{0.56, 0.58, 0.6, 0.62\}$, which is a realistic range for the volume fractions achievable by electrode calendering during manufacturing. The different probability density functions P of the sphere radii used are shown in Figure 7. They are constructed as follows. The function labeled $P_{0,\text{mono}}$ is the density of a log-normal distribution and corresponds to the one fitted to the measured image data. The functions $P_{-1,\text{mono}}$ and $P_{1,\text{mono}}$ are also densities of log-normal distributions, but their mean values are 1 µm lower and higher than that of $P_{0,\text{mono}}$, respectively. The remaining probability densities $P_{-0.5,\text{bi}}$, $P_{0,\text{bi}}$ and $P_{0.5,\text{bi}}$ are convex combinations of the form $(1-\lambda)P_{-1,\text{mono}} + \lambda P_{1,\text{mono}}$ with $\lambda \in \{0.25, 0.5, 0.75\}$. The shift of their mean values with respect to the original density $P_{0,\text{mono}}$ is -0.5 µm, 0 µm and 0.5 µm, respectively. This corresponds to the use of a mixture of sphere radii drawn from $P_{-1,\text{mono}}$ and $P_{1,\text{mono}}$, resulting in bimodal density functions.

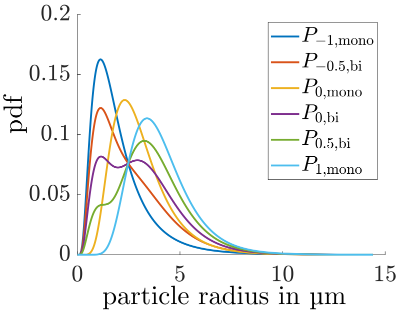

FIGURE 7. Probability density functions of different (number-weighted) sphere radius distributions used for the generation of virtual cathode microstructures.

For each of the four values for the packing density p and the six different densities P of sphere radii, we generate three model realizations, which results in a total of 24 different parameter constellations and a total of 72 model realizations with a size of $500 \times 500 \times 500$ voxels each, see Figure A2 for examples of 2D slices of different model realizations.

Figure 8 shows the mean values of the geometric descriptors estimated from the model realizations for each of the 24 model parameter specifications. Note that while the chosen particle size distributions are ordered so that their mean values are increasing, there is no strictly monotonous relation between the distributions themselves, as a bi-modal probability distribution exhibits a larger variance than a mono-modal distribution with the same mean value.

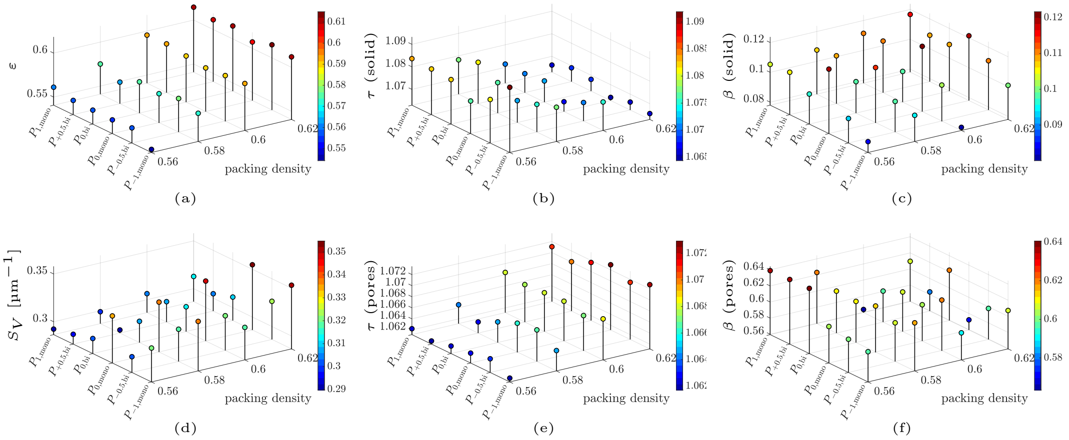

(a) (b) (c)

(d) (e) (f)

FIGURE 8. Values of geometric descriptors estimated from model realizations for the 24 different parameter constellations considered in this study: for volume fraction (a), mean geodesic tortuosity of the solid (b) and pore phase (e), constrictivity of the solid (c) and pore phase (f) as well as specific surface area (d).

The volume fraction ε of the solid phase clearly depends only on the packing density p, with some minor variations across the various particle size distributions. Recall that p is a parameter of the stochastic 3D model used to control the targeted volume fraction, while the value of ε is estimated from realizations of the stochastic model. Due to minor overlaps between generated particles, the value of ε can be slightly lower than the packing density p. The mean geodesic tortuosity τ remains also fairly consistent across varying particle size distributions, with some stronger fluctuations in the case of the solid phase. The specific surface area S_V is generally larger for higher packing densities and smaller mean particle radii. However, the dependence of S_V on particle size distribution and packing density is not consistently monotone. The constrictivity β shows a slight positive correlation with the volume fraction of the considered phase, which has already been reported in a previous study on virtual materials testing [51].

Figure 9 shows the values of k_{eff} determined by the RNM from model realizations for each of the 24 parameter specifications. Given the size of this data base, using TauFactor, it would not be possible to determine the M-factor for every realization in a reasonable amount of time. Similarly to Figure 8, it can be observed that there is no strictly monotone relationship with respect to the different particle size distributions. For the solid phase, the effective conductivity values are primarily influenced by the packing density p. In particular, increasing the packing density from 0.56 to 0.62 increases the effective conductivity of model realizations on average by 35.51%, whereas the maximum relative difference between effective conductivities of model realizations that use different particle size distributions is on average only 10.67%. There is also a tendency for realizations with higher mean particle size to show a higher effective conductivity, although this behavior is not consistently true. For the pore phase, the effective conductivity values for model realizations with the lowest packing density of 0.56 are on average 18.16%

higher than those for realizations with the highest packing density of 0.62. The maximum relative difference between model realizations using different particle size distributions is on average 12.35%. When these relative differences are compared to those determined for the solid phase, the chosen particle size distribution seems to have a larger relative impact on the values of effective conductivity of the (electrolyte-filled) pore phase, whereas the packing density has a larger impact on the values of effective conductivity of the solid phase. Similarly to the solid phase, there is also an indication of an inverse monotone relationship between the mean particle size and the values of effective conductivity.

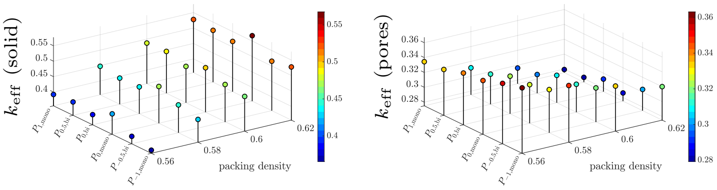

(a) (b)

FIGURE 9. Values of the effective conductivity of the solid phase (a) and the (electrolyte-filled) pore phase (b) determined by the RNM from model realizations for each of the 24 parameter specifications.

4.4. **Structure-property relationships.** Using the data base of virtual cathode structures described in Section 4.3, we now aim to investigate quantitative structure-property relationships by which the M-factor can be expressed by geometric descriptors of the given material phase. In particular, we aim to assess the quality of the previously established relationship

$$\widehat{M} = \frac{\varepsilon^{1.67-0.48\beta}}{\tau^{5.18}}, \tag{7}$$

between the M-factor and three different geometric descriptors, see [11]. Here, as in the preceding sections of the present paper, ε, β, and τ denote the volume fraction, the constrictivity, and the mean geodesic tortuosity of the phase under consideration, that is, the solid phase or the pore phase. The relationship stated in Eq. (7) was derived in [11] based on virtually generated structures that exhibit a wide range of different morphologies.

First, we investigate the fit of $\widehat{M}$ defined in Eq. (7) based on the experimentally measured tomographic image data described in Section 2, where we use the M-factor values determined by TauFactor through Eq. (4) as ground-truth. The resulting predictions are shown in Figure 10, where the values of $\widehat{M}$ and the ground-truth values obtained for M by TauFactor are plotted on the x- and y-axis, respectively. Recall that the values for M obtained by TauFactor and the values for the geometric descriptors ε, β and τ appearing on the right-hand side of Eq. (7) have already been visualized as part of Figure 3.

As we can see in Figure 10, there is a slight additive error for the values of $\widehat{M}$ computed for the pore phase, which is visualized by the parallel shift of the red diamonds with respect to the diagonal line through the origin. Similarly, a multiplicative error is observed for the values of $\widehat{M}$ computed for the solid phase, visible by the increased slope of the blue point cloud compared to the slope of the line through the origin. Nevertheless, Eq. (7) gives an overall accurate prediction of the M-factor for both phases, even though the coefficients in Eq. (7) have been taken from [11] and not adjusted for the new data set considered in the present paper.

Finally, we investigate how well the predictions for the M-factor by $\widetilde{M}$ and $\widehat{M}$, given in Eqs. (6) and (7), generalize within the framework of our variation study. For each model realization generated as described in Section 4.3, we computed the estimated values of the geometric descriptors stated in Section 3.2, see also Figure 8. Then, using Eq. (7), we obtain an estimate $\widehat{M}$ of the M-factor for each realization of the stochastic 3D model. On the other hand,

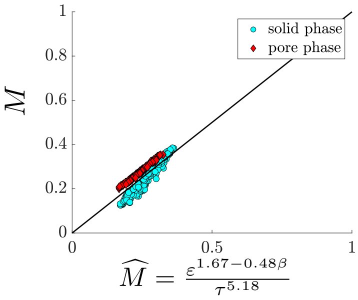

FIGURE 10. Predicting the M-factor based on geometric descriptors computed from tomographic image data.

for the same model realization, we obtain an estimate $\widetilde{M}$ of the M-factor using the resistor network method. For this, we determine the connectivity graph of each model realization as described in Section 3.4.1. This graph is then used to determine the effective conductivity k_{eff} by the RNM, which is corrected by the factor c determined in Section 4.2.2. Thus, we obtain estimated values $\widehat{M}$ and $\widetilde{M}$ of the M-factor for every model realization of the variation study, see Figure 11.

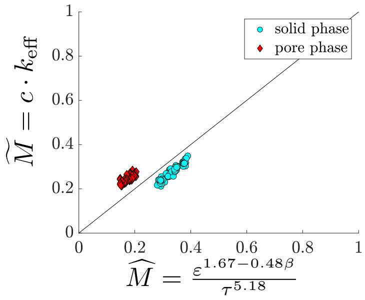

FIGURE 11. Comparison of the estimated values $\widetilde{M}$ and $\widehat{M}$ of the M-factor, determined by RNM and by geometric descriptors, respectively, based on virtual structures generated by the stochastic 3D model.

Although there are some deviations between the estimated values $\widetilde{M}$ and $\widehat{M}$, the overall trend is largely in agreement, especially considering the reduced degree of abstraction that $\widetilde{M}$ and $\widehat{M}$ have undergone compared to the original approach to compute the M-factor by TauFactor through Eq. (4). More precisely, the coefficients of the empirical regression model $\widehat{M}$ given in Eq. (7) have been estimated in a previous work [11] based on tomographic image data of differently manufactured cathodes in lithium-ion batteries. Furthermore, to determine $\widetilde{M}$, the correction factor c appearing in Eq. (6) has also been estimated based on tomographic image data of experimentally manufactured cathodes. In both cases, the procedures for computing $\widetilde{M}$ and $\widehat{M}$ have not been adapted to the varying particle size distributions and packing densities of the virtual structures considered in Section 4.3. However, as shown in Figure 11, the values obtained for $\widetilde{M}$ and $\widehat{M}$ agree well with each other and mutually validate the prediction power of $\widetilde{M}$ and $\widehat{M}$.

5. CONCLUSION

In this paper, a parametric stochastic microstructure model has been fitted to nine differently manufactured cathodes based on 3D image data acquired by synchrotron tomography.

The goodness of model fit has been validated by comparing the values of various geometric descriptors of model realizations that have not been used for model calibration to those obtained for tomographic image data. Based on the parametric nature of the model, it was possible to specifically adjust aspects of the virtually generated structures by systematically varying the corresponding model parameters. In particular, we varied the particle size distribution and the packing density in order to generate virtual but realistic cathode structures with varying morphologies. Using the data base of virtual cathode structures obtained in this way, we investigated structure-property relationships between geometric descriptors that characterize the morphology of the microstructure and macroscopic effective transport properties that quantify the performance of the cathode at the electrode scale. For this purpose, we used the resistor network method for a fast and efficient computation of effective conductivity, given by the so-called M-factor, based on a connectivity graph of the microstructure. The accuracy of this approach has been assessed on experimentally measured tomographic image data by comparing the resulting values of the M-factor to those obtained by the more costly approach of directly solving the partial differential equation corresponding to steady-state diffusive flow through the material phase under consideration. On the other hand, we also considered an estimate for the M-factor based on geometric descriptors that was already established in a previous paper. Both estimates have been compared with each other based on the data set of virtual cathode structures generated by means of the stochastic microstructure model. The results obtained showed good agreement between the two methods for estimating the M-factor, which validates both the results of the RNM approach and those obtained by structure-property relationships.

Data availability

The datasets generated and/or analyzed during the current study are available from the corresponding author on reasonable request.

Code availability

All formulations and algorithms necessary to reproduce the results of this study are described in the Methods and Results sections.

Acknowledgments

This research was supported by the German Federal Ministry for Economic Affairs and Energy (BMWE) and granted through Project Management Jülich (03ETE039G, 03ETE039J, 03ETE039H).

Credit authorship contribution statement

Phillip Gräfensteiner: Conceptualization, Data curation, Formal analysis, Investigation, Methodology, Software, Validation, Visualization, Writing–original draft, Writing–review & editing. **Alexandra Pamperin:** Conceptualization, Data curation, Investigation, Methodology, Software, Validation, Writing–original draft, Writing–review & editing. **Markus Osenberg:** Data curation, Investigation, Resources, Writing–review & editing. **Rasmus Himstedt:** Investigation, Resources, Writing–review & editing. **Matthias Neumann:** Methodology, Software, Writing–review & editing. **Benedikt Prifling:** Methodology, Software, Writing–review & editing. **Ingo Manke:** Funding acquisition, Project administration, Resources, Writing–review & editing. **Marc Kamlah:** Funding acquisition, Project administration, Supervision, Writing–review & editing. **Volker Schmidt:** Funding acquisition, Project administration, Supervision, Writing–review & editing.

Competing interests

The authors declare that they have no competing financial or non-financial interests.

REFERENCES

[1] R. Korthauer. *Lithium-Ion Batteries: Basics and Applications.* Springer, 2018.

[2] S. N. Chiu, D. Stoyan, W. S. Kendall and J. Mecke. *Stochastic Geometry and its Applications.* J. Wiley & Sons, 3rd edition, 2013.

[3] D. Jeulin. *Morphological Models of Random Structures.* Springer, 2021.

[4] S. Barman and D. Bolin. A three-dimensional statistical model for imaged microstructures of porous polymer films. *Journal of Microscopy*, 269:247–258, 2018.

[5] M. Neumann, P. Gräfensteiner, C. Santos De Oliveira, J. Martins De Souza E Silva, S. Koppka, D. Enke, P. Huber and V. Schmidt. Morphology of nanoporous glass: Stochastic 3D modeling, stereology and the influence of pore width. *Physical Review Materials*, 8: 045605, 2024.

[6] P. Gräfensteiner, M. Osenberg, A. Hilger, N. Bohn, J. R. Binder, I. Manke, V. Schmidt and M. Neumann. Data-driven stochastic 3D modeling of the nanoporous binder-conductive additive phase in battery cathodes. *Journal of Mathematics in Industry*, 15:9, 2025.

[7] S. Weber, B. Prifling, R. K. Jeela, A. Prahs, D. Schneider, B. Nestler and V. Schmidt. A time-continuous approach to analyzing anode aging in solid-oxide fuel cells via stochastic 3D microstructure modeling and physics-based simulations. *Computational Materials Science*, 264:114491, 2026.

[8] P. Gräfensteiner, E. Löwer, O. Furat, U. A. Peuker and V. Schmidt. Artificial filter cake generation: Digital twins via stochastic 3D modeling based on µ-CT image data. *Powder Technology*, 452:120550, 2025.

[9] S. Barman, H. Rootzén and D. Bolin. Prediction of diffusive transport through polymer films from characteristics of the pore geometry. *AIChE Journal*, 65:446–457, 2019.

[10] P. Gräfensteiner, A. Rodriguez, P. Leitl, E. Baikova, M. Fuchs, E. Machado Charry, U. Hirn, A. Hilger, I. Manke, R. Schennach, M. Neumann, V. Schmidt and K. Zojer. Predicting air flow in calendered paper sheets from µ-CT data: Combining physics with morphology. *Transport in Porous Media*, 153:15, 2026.

[11] M. Neumann, O. Stenzel, F. Willot, L. Holzer and V. Schmidt. Quantifying the influence of microstructure on effective conductivity and permeability: Virtual materials testing. *International Journal of Solid and Structures*, 184:211–220, 2020.

[12] B. Prifling, M. Röding, P. Townsend, M. Neumann and V. Schmidt. Large-scale statistical learning for mass transport prediction in porous materials using 90,000 artificially generated microstructures. *Frontiers in Materials*, 8:786502, 2021.

[13] L. Holzer, P. Marmet, M. Fingerle-Straß, A. Wiegmann, M. Neumann and V. Schmidt. *Tortuosity and Microstructure Effects in Porous Media: Classical Theories, Empirical Data and Modern Methods.* Springer, 2023.

[14] J. Landesfeind, J. Hattendorff, A. Ehrl, W. A. Wall and H. A. Gasteiger. Tortuosity determination of battery electrodes and separators by impedance spectroscopy. *Journal of The Electrochemical Society*, 163:A1373, 2016.

[15] S. J. Cooper, A. Bertei, P. R. Shearing, J. A. Kilner and N. Brandon. Taufactor: An open-source application for calculating tortuosity factors from tomographic data. *SoftwareX*, 5: 203–210, 2016.

[16] J. C. Ferguson, F. Panerai, A. Borner and N. N. Mansour. PuMA: the Porous Microstructure Analysis software. *SoftwareX*, 7:81–87, 2018.

[17] T. Tranter, M. Kok, M. Lam and J. Gostick. pytrax: A simple and efficient random walk implementation for calculating the directional tortuosity of images. *SoftwareX*, 10:100277, 2019.

[18] Math2Market GmbH. GeoDict, 2026. URL `http://www.geodict.com`.

[19] Thermo Fisher Scientific, Inc. Avizo, 2026. URL `http://www.avizo3d.com`.

[20] Synposys, Inc. Simpleware, 2026. URL `https://www.synopsys.com/simpleware.html`.

[21] O. Birkholz, Y. Gan and M. Kamlah. Modeling the effective conductivity of the solid and the pore phase in granular materials using resistor networks. *Powder Technology*, 351: 54–65, 2019.

[22] O. Birkholz, M. Neumann, V. Schmidt and M. Kamlah. Statistical investigation of structural and transport properties of densely-packed assemblies of overlapping spheres using the resistor network method. *Powder Technology*, 378:659–666, 2021.

[23] H. Markötter, M. Sintschuk, R. Britzke, S. Dayani and G. Bruno. Upgraded imaging capabilities at the BAMline (BESSY II). *Journal of Synchrotron Radiation*, 29:1292–1298, 2022.

[24] H. Markötter, B. R. Müller, A. Kupsch, S. Evsevleev, T. Arlt, A. Ulbricht, S. Dayani and G. Bruno. A review of X-ray imaging at the BAMline (BESSY II). *Advanced Engineering Materials*, 25:2201034, 2023.

[25] L. I. Rudin, S. Osher and E. Fatemi. Nonlinear total variation based noise removal algorithms. *Physica D: Nonlinear Phenomena*, 60:259–268, 1992.

[26] D. Gürsoy, F. De Carlo, X. Xiao and C. Jacobsen. TomoPy: a framework for the analysis of synchrotron tomographic data. *Journal of Synchrotron Radiation*, 21:1188–1193, 2014.

[27] B. A. Dowd, G. H. Campbell, R. B. Marr, V. V. Nagarkar, S. V. Tipnis, L. Axe and D. P. Siddons. Developments in synchrotron X-ray computed microtomography at the national synchrotron light source. In U. Bonse, editor, *Developments in X-ray Tomography II*, volume 3772, pages 224–237. International Society for Optics and Photonics, 1999.

[28] J. Schindelin, I. Arganda-Carreras, E. Frise, V. Kaynig, M. Longair, T. Pietzsch, S. Preibisch, C. Rueden, S. Saalfeld, B. Schmid, J.-Y. Tinevez, D. White, V. Hartenstein, K. Eliceiri, P. Tomancak and A. Cardona. Fiji: An open-source platform for biological-image analysis. *Nature Methods*, 9:676–82, 2012.

[29] P. Soille. *Morphological Image Analysis: Principles and Applications.* Springer, 2004.

[30] J. B. T. M. Roerdink and A. Meijster. The watershed transform: definitions, algorithms and parallelization strategies. *Fundamenta Informaticae*, 41:187–228, 2000.

[31] J. Zheng and R. D. Hryciw. Segmentation of contacting soil particles in images by modified watershed analysis. *Computers and Geotechnics*, 73:142–152, 2016.

[32] J. Serra. *Image Analysis and Mathematical Morphology.* Academic Press, 1982.

[33] L. Vincent. Morphological grayscale reconstruction: Definition, efficient algorithm and applications in image analysis. In *Proceedings of 1992 IEEE Computer Society Conference on Computer Vision and Pattern Recognition*, pages 633–635. IEEE Computer Society, 1992.

[34] C. R. Maurer, R. Qi and V. Raghavan. A linear time algorithm for computing exact Euclidean distance transforms of binary images in arbitrary dimensions. *IEEE Transactions on Pattern Analysis and Machine Intelligence*, 25:265–270, 2003.

[35] D. Westhoff, I. Manke and V. Schmidt. Generation of virtual lithium-ion battery electrode microstructures based on spatial stochastic modeling. *Computational Materials Science*, 151:53–64, 2018.

[36] B. Prifling, D. Westhoff, D. Schmidt, H. Markötter, I. Manke, V. Knoblauch and V. Schmidt. Parametric microstructure modeling of compressed cathode materials for Li-ion batteries. *Computational Materials Science*, 169:109083, 2019.

[37] J. Mościński, M. Bargieł, Z. A. Rycerz and P. W. M. Jakobs. The force-biased algorithm for the irregular close packing of equal hard spheres. *Molecular Simulation*, 3:201–212, 1989.

[38] A. Bezrukov, M. Bargieł and D. Stoyan. Statistical analysis of simulated random packings of spheres. *Particle & Particle Systems Characterization*, 19:111–118, 2002.

[39] A. Lang and C. Schwab. Isotropic Gaussian random fields on the sphere: Regularity, fast simulation and stochastic partial differential equations. *The Annals of Applied Probability*, 25:3047–3094, 2015.

[40] M. L. Eaton. *Multivariate Statistics. A Vector Space Approach.* J. Wiley & Sons, 1983.

[41] N. Otsu. A threshold selection method from gray-level histograms. *IEEE Transactions on Systems, Man, and Cybernetics*, 9:62–66, 1979.

[42] J. Ohser and K. Schladitz. *3D Images of Materials Structures: Processing and Analysis.* Wiley-VCH, 2009.

[43] Jungnickel, Dieter. *Graphs, Networks and Algorithms*, volume 5 of *Algorithms and Computation in Mathematics.* Springer-Verlag, 2005.

[44] W. Feller. *An Introduction to Probability Theory and Its Applications.* J. Wiley & Sons, 1968.

[45] R. B. Bird, W. E. Stewai and E. N. Lightfoot. *Transport Phenomena.* J. Wiley & Sons, revised 2nd edition, 2007.

[46] D. J. Griffiths. *Introduction to Electrodynamics.* Cambridge University Press, 2023.

[47] C. Redenbach. Microstructure models for cellular materials. *Computational Materials Science*, 44:1397–1407, 2009.

[48] M. Neumann, M. Ademmer, M. Osenberg, A. Hilger, F. Wilde, S. Muench, M. D. Hager, U. S. Schubert, I. Manke and V. Schmidt. 3D microstructure characterization of polymer battery electrodes by statistical image analysis based on synchrotron X-ray tomography. *Journal of Power Sources*, 542:231783, 2022.

[49] W. S. Jodrey and E. M. Tory. Computer simulation of close random packing of equal spheres. *Physical Review A*, 32:2347, 1985.

[50] Y. Gan, M. Kamlah and J. Reimann. Computer simulation of packing structure in pebble beds. *Fusion Engineering and Design*, 85:1782–1787, 2010.

[51] M. Neumann, J. Staněk, O. M. Pecho, L. Holzer, V. Beneš and V. Schmidt. Stochastic 3D modeling of complex three-phase microstructures in SOFC-electrodes with completely connected phases. *Computational Materials Science*, 118:353–364, 2016.

[52] J. Feinauer, T. Brereton, A. Spettl, M. Weber, I. Manke and V. Schmidt. Stochastic 3D modeling of the microstructure of lithium-ion battery anodes via Gaussian random fields on the sphere. *Computational Materials Science*, 109:137–146, 2015.

APPENDIX

We provide additional information on some aspects of the manuscript.

A.1. **Material composition.** Table A1 shows an overview of the different compositions of the conductive binder-additive mixture used in the three recipes. Table A2 shows the recipe used for each sample considered in this study, along with experimentally measured information used to obtain a binarization of the tomographic grayscale image data as described in Section 2.3 of the main text.

recipe	1	2	3
active material (NMC83)	0.965	0.973	0.972
carbon black (C45)	0.015	0.015	0.015
PVDF binder (Solef 5140)	0.012	0.012	0.012
multi-wall carbon nanotubes	0.008	0	0
single-wall carbon nanotubes	0	0	0.001

TABLE A1. Recipe information for conductive binder-additive mixture used for the cathode samples considered in this study. All numbers are given as mass-weighted percentages.

sample number	1	2	3	4	5	6	7	8	9
thickness [µm]	126	118	112	129	119	115	130	120	115
mass loading [$\mathrm{mg\,cm^{-2}}$]	15.7	15.3	15.5	15.1	15.3	15.4	15.3	15.3	15.4
density [$\mathrm{g\,cm^{-3}}$]	2.83	2.96	3.21	2.64	2.93	3.07	2.68	2.93	3.09
volume fraction	0.556	0.582	0.631	0.514	0.571	0.599	0.526	0.575	0.607
binder-additive recipe	1	1	1	2	2	2	3	3	3

TABLE A2. Overview of cathode samples and porosities, thickness is total electrode thickness (including substrate). See Table A1 for more information on the conductive binder-additive mixture recipe

A.2. **Parameters of the stochastic microstructure model.** We list formulas and values for the parameters of the stochastic microstructure model described in Section 3.1. All values are given with respect to voxel units. The angular power spectrum of the Gaussian random fields has been modeled by the function

$$A_\ell = \frac{c_1\ell + c_2}{\ell^2 + c_3\ell + c_4} \tag{8}$$

for each $\ell \in \mathbb{N}_0$, where the values $c_1 = 0.2018$, $c_2 = 0.1818$, $c_3 = -3.67$ and $c_4 = 3.559$ have been determined by a least squares approach based on the values estimated from tomographic image data, following the same approach as in [52]. The series expansion of the Gaussian random field shown in Eq. (2) of the main text was approximated up to a degree of $L = 7$. The particle size distribution used to generate digital twins of physical samples has been modeled by a log-normal distribution, with probability density given by

$$P(x) = \frac{1}{x\sigma\sqrt{2\pi}} \exp\left(-\frac{(\ln x - \mu)^2}{2\sigma^2}\right), \tag{9}$$

for each $x \in (0, \infty)$, where the values $\mu = 2.0498$ and $\sigma = 0.43898$ have been estimated based on all particles observed in the available tomographic image data. The distance threshold d was chosen to be equal to 3.2 for all samples. Values of the packing density p and the correction factor ρ used are listed in Table A3. These values are used to generate digital twins of physical samples with a given volume fraction, as presented in Section 4.1. In the context of the variation study presented in Section 4.3, the correction factor ρ is equal to 1.

sample number	1	2	3	4	5	6	7	8	9
packing density p	0.556	0.582	0.631	0.515	0.571	0.598	0.526	0.575	0.607
correction factor ρ	1.0055	1.0064	1.0098	1.0034	1.0057	1.0077	1.0039	1.0060	1.0083

Table A3. Values of the packing density and correction factor used to generated realizations of the stochastic microstructure model for a given sample.

A.3. **The RNM on idealized geometries.** We provide additional information on the study comparing the values of the M-factor as determined by RNM and by TauFactor presented in Section 4.2.1. Table A4 shows the parameters used to generate the eight different overlapping sphere assemblies, which are the basis for analysis performed in Section 4.2.1. The order of the rows from top to bottom is the same as the visualizations in Figures 4b and 4c from left to right. Figure A1 shows the resulting histograms of contact areas between particles, determined analytically and estimated based on discretized image data as discussed in Section 3.4.1. These histograms show the values aggregated over all eight sphere assemblies.

Setting	mca	particle radii in voxel	probability vector
1	10°	26.7	1
2	10°	[20.1, 23.3, 26.5, 29.6, 32.8]	[0.0347, 0.2389, 0.4527, 0.2389, 0.0347]
3	10°	[13.4, 19.6, 25.8, 31.9, 38.1]	[0.0347, 0.2389, 0.4527, 0.2389, 0.0347]
4	10°	[6.90, 15.8, 24.6, 33.5, 42.4]	[0.0347, 0.2389, 0.4527, 0.2389, 0.0347]
5	15°	26.7	1
6	15°	[20.1, 23.3, 26.5, 29.6, 32.8]	[0.0347, 0.2389, 0.4527, 0.2389, 0.0347]
7	15°	[13.4, 19.6, 25.7, 31.9, 38.1]	[0.0347, 0.2389, 0.4527, 0.2389, 0.0347]
8	15°	[6.92, 15.8, 24.7, 33.6, 42.5]	[0.0347, 0.2389, 0.4527, 0.2389, 0.0347]

Table A4. Particle size distributions and mean contact angles used to generate the 8 different assemblies of overlapping spheres for the comparison between TauFactor and RNM in Section 4.2.1 of the main text.

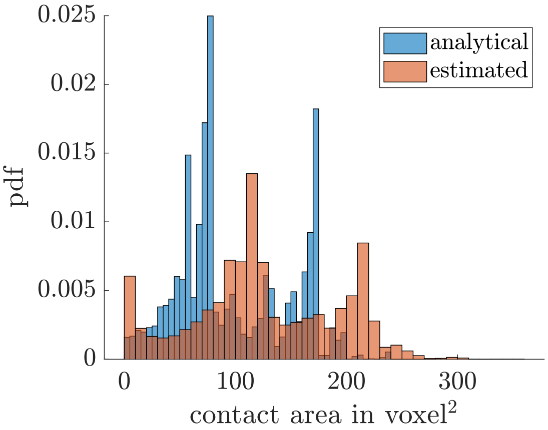

Figure A1. Histograms of contact area distribution between particles in idealized spherical geometries, determined analytically (blue) and estimated based on discretized image data (orange).

A.4. **Variation study.** Figure A2 shows examples of 2D slices of virtual cathode structures generated by the stochastic microstructure model in the context of the variation study presented in Section 4.3 of the main text.

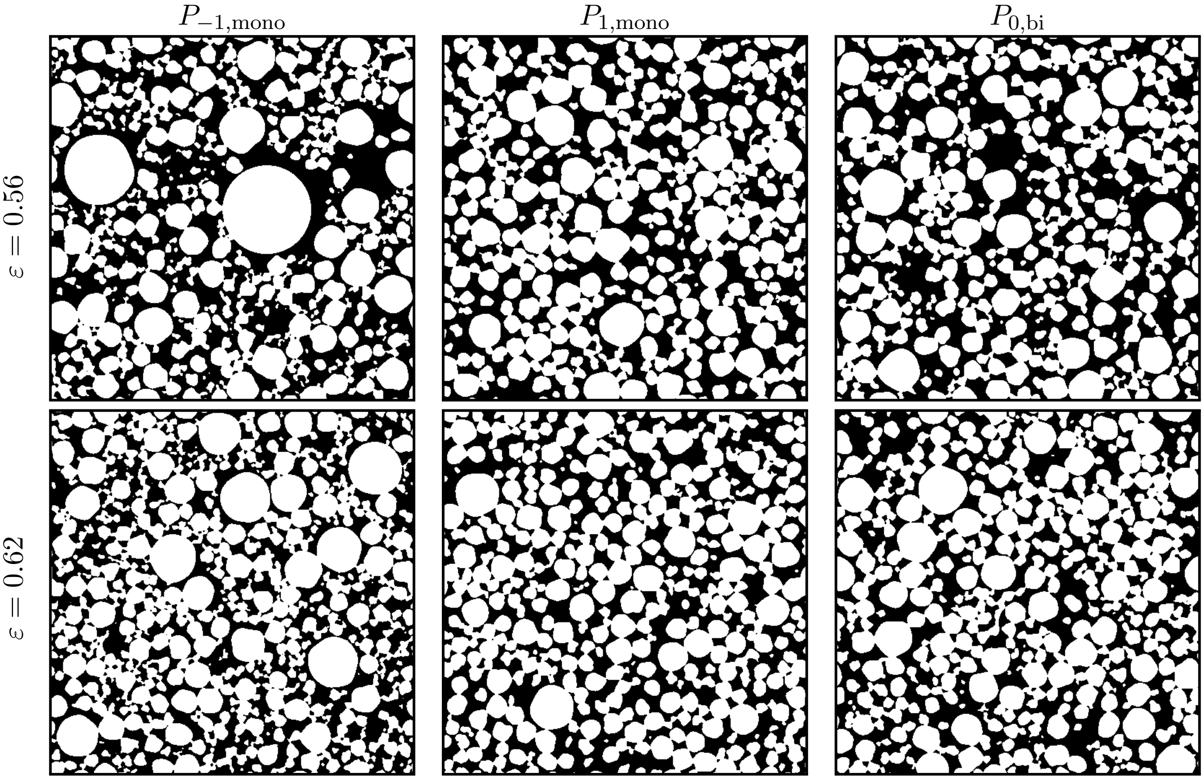

Figure A2. Examples of 2D slices of virtual cathode structures generated by the stochastic 3D model. Images presented in upper and lower rows correspond to different values of volume fraction of active material particles, while different particle size distributions have been used for the images in different columns.